ELSEVIER

Corrosion behaviour of powder metallurgical and cast Al–Zn–Mg base alloys

A.V. Sameljuk [*], O.D. Neikov, A.V. Krajnikov, Yu.V. Milman, G.E. Thompson [1]

Frantsevich Institute for Problems of Material Science, 3 Krzhizhanivsky St., Kiev 03142, Ukraine

Abstract

The behaviour of Al–Zn–Mg base alloys produced by powder metallurgy and casting has been studied using potentiodynamic polarisation in 0.3% and 3% NaCl solutions. The influence of alloy production route on microstructure has been examined by scanning electron microscopy, Auger electron spectroscopy and secondary ion mass spectrometry. An improvement in performance of powder metallurgy (PM) materials, compared with the cast alloy, was evident in solutions of low chloride concentration; less striking differences were revealed in high chloride concentration. Both powder metallurgy and cast alloys show two main types of precipitates, which were identified as Zn–Mg and Zr–Sc base intermetallic phases. The microstructure of the PM alloys is refined compared with the cast material, which assists understanding of the corrosion performance. The corrosion process commences with dissolution of the Zn–Mg base phases, with the relatively coarse phases present in the cast alloy showing ready development of corrosion.
© 2003 Elsevier Ltd. All rights reserved.

Keywords: Aluminium (A); Polarisation (B); SEM (B); Pitting corrosion (C)

[*] Corresponding author. Fax: +380-44-4442131.

E-mail address: leza@materials.kiev.ua (A.V. Sameljuk).

[1] Corrosion and Protection Centre, University of Manchester Institute of Science and Technology, P.O. Box 88, Manchester M60 1QD, UK.

1. Introduction

Al–Mg–Zn base alloys, with their combination of good strength, corrosion resistance and weldability, show promise for further improvement by additional alloying with transition metals [1,2]. However, traditional metallurgical approaches are restricted through the limited solubilities of many of the principal alloying elements, including Zr, Sc, Ti, Ni, etc, in the aluminium matrix. This limitation may be overcome with the use of rapid solidification (RS) technologies, which provide much higher solubilities, refined microstructures, reduced segregation and eliminate coarsely precipitated intermetallic compounds [3,4]. For example, Al–Mg–Zn base alloys with high levels of tensile strength have been produced recently by water atomisation followed by powder compacting [5,6].

Whereas mechanical properties may be improved through increase of alloying element concentrations followed by precipitation, such procedures frequently increase susceptibility of the alloy to localised corrosion. This is usually due to an increased volume fraction of second phase precipitates [7,8]. Rapid solidification extends solubility but, however, does not eliminate completely precipitation. In this paper, the corrosion behaviour of an Al–Mg–Zn base alloy, produced by powder metallurgy (PM) and by casting, is examined using electrochemical measurements and microstructural studies of the alloys before and after corrosion testing.

2. Experimental

The composition of the Al–Zn–Mg alloy is given in Table 1. The production of the cast alloy involved the following: the melt, prepared in an induction furnace, issued through a hole at the base of the crucible to water-cooled, copper moulds of 25 mm diameter and 100 mm height. The cooling rate of the melt was ∼45 K/s.

The PM alloy production was based on water atomisation technology [5] and comprised the following steps: (1) preparation of the charge for melting using master alloys, (2) melting in an induction furnace, (3) atomising of the melt by jets of high-pressure cooled water with cooling rates of about 10^6 K/s, (4) filtration of the suspension of the atomised metal in water under vacuum, (5) drying of a thin layer of the wet powder with continuous intermixing, (6) cold-pressing of the dried powders into compacts of 30% porosity, (7) degassing of the green compacts under vacuum at elevated temperature, (8) consolidation of the pre-forms by vacuum hot pulse pressing with impulse loading of 1 GPa, and, on completion, (9) hot extrusion with an extrusion ratio of 17.

Table 1
Chemical composition of the selected alloy (wt.%)

Zn	Mg	Zr	Mn	Sc	Al
5	3	0.7	0.5	0.3	Balance

Heating and deformation of the powder during the consolidation stages influences the original RS microstructure. In order to separate contributions of RS and compacting conditions, both cold-pressed (stage 6) and hot-extruded (stage 9) samples were used for corrosion studies. Cast, cold-pressed and extruded samples were polished with diamond (3.2 μm) paste under similar conditions, followed by ultrasonic cleaning in acetone.

Electrochemical measurements were conducted with an EG&G Princeton Applied Research Versastat II instrument controlled by the PAR Model 352 software. A three-electrode cell with a platinum counter electrode and a silver/silver chloride (SSC) reference electrode were used. All tests were performed in aqueous solutions 0.3% (0.051 M) and 3 wt.% (0.51 M) NaCl. The solutions were not deaerated. The reference electrode was separated from the cell by a Vycor frit. Before measurements, specimens were held in the test solution for 1 h to establish a steady open circuit corrosion potential, E_{corr}. Potentialodynamic polarisation scans were performed at a relatively slow scan rate of 0.5 mV/s, commencing from a potential 0.1 V below E_{corr}. All experiments were conducted at room temperature without temperature control; the solution volume was 250 ml and a Teflon knife-edge O-ring was used to expose a specimen area of 1 cm^2.

Cast, cold-pressed and extruded samples in initial state and after corrosion tests (full polarisation run) in NaCl were used to study corrosion-induced changes of alloy microstructure. In addition, as-atomised powder was put into water at pH = 6 for a month to compare material behaviour in water and salt solutions.

The surfaces of individual powder particles were studied by Auger electron spectroscopy (AES) and secondary ion mass-spectrometry (SIMS). A JAMP-I0S scanning Auger microprobe with a primary electron beam (energy 10 keV and current 10 nA) of 1 μm diameter was used to study powder surface chemistry. Auger spectra were recorded in the derivative mode. In order to characterise the surface concentration of element i, the relative Auger peak height ratios, $r_i = I_i/I_{Al}$, were monitored. Here, I_{Al} represents the peak-to-peak height of Al (KLL 1396 eV) and I_i is the peak-to-peak height of element i. Depth profiles were obtained using argon at 8 mPa pressure to sputter sequentially atomic layers with an accelerating voltage of 3 kV. The sputtering rate was estimated from sputtering a SiO_2 film of known thickness.

Dynamic SIMS measurements were performed using a CAMECA ims 5f instrument incorporating a double focusing sector field mass spectrometer. Positive secondary ions were used for in-depth analysis of the distributions of metallic species. An O_2^+ primary beam, at an accelerating voltage of 12.55 kV and primary ion current of 3–13 nm, was scanned over an area of 35 × 35 μm. The sputter rate was calibrated from sputtering an aluminium foil of known thickness. Possible differences in sputtering rates between individual measurements, caused by the fluctuations of the primary ion current, were corrected by adjustment of the current values to the maximum current used as a reference value. A mass resolution, $m/\Delta m$, of 300 was used for all measurements. Intensities of peaks were normalised to the intensity of the most intense [27]Al peak to compensate for various geometric factors that influence the peak intensities.

A JSXA Superprobe-733 electron microprobe, operating at 25 kV, with a beam current of 20 nA, was used to examine surface structure and distributions of the main alloying elements (Mg, Zn, Zr, Sc and Mn) across a selected powder particle and between individual particles on the micron scale. Secondary (SE) and back-scattered electron (BE) images were used for microstructural studies. Point by point electron probe microanalyses (EPMAs) were performed and elemental profiles and maps were recorded using the relevant K_α and L_α lines and by wavelength dispersive detection.

3. Results

3.1. Corrosion behaviour

The results of corrosion measurements in 0.3% and 3% NaCl solutions are summarised in Fig. 1a and b respectively. At a low NaCl concentration, corrosion potentials for all three samples were similar, in the range −700 to 715 mV (SSC). A passive region, extending over a potential range of 1600 mV, with a corrosion current density of about 10^{-6} A/cm^2, was evident for the cold-pressed material. The pitting potential was not achieved over the selected potential range employed. The corrosion behaviour of the extruded material is generally similar to that of the cold-
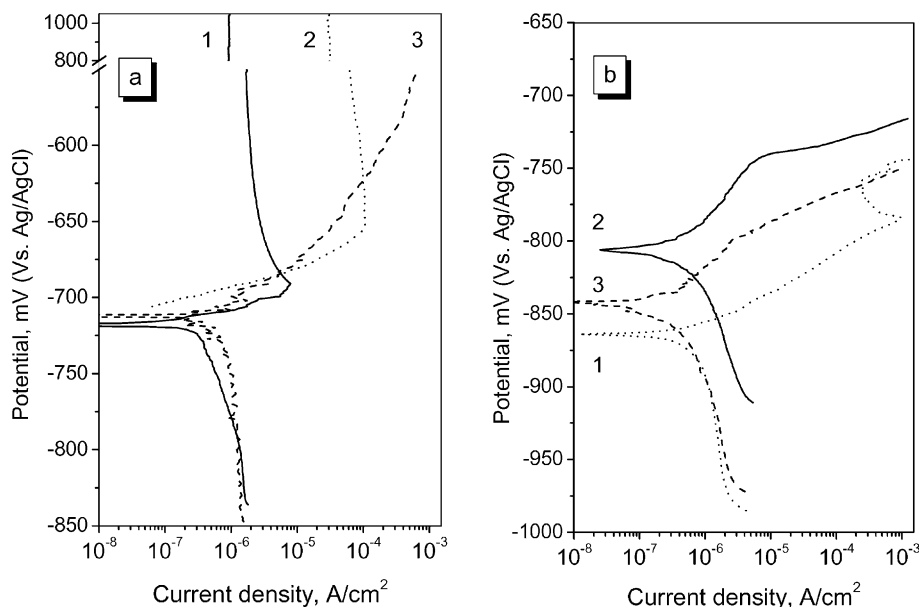

Fig. 1. Polarisation curves for cold-pressed (1), extruded (2) and cast (3) alloys in solutions of different concentration of sodium chloride. A sweep rate of 0.5 mV/s, commencing from 0.1 V below the corrosion potential was employed: (a) 0.3 wt.% NaCl; (b) 3.0 wt.% NaCl.

pressed powder (Fig. 1a), revealing a wide passive range, but the current density $(3 \times 10^{-5}$ A/cm^2) is greater than that for the cold-pressed material. Unlike the PM samples, the cast material undergoes localised corrosion from the commencement of anodic polarisation.

An increase of the chloride concentration changes the electrochemical behaviour of the alloy materials, with a decrease of the corrosion potential of 110–140 mV revealed for all alloy samples. Further, pitting potentials are now evident for the cold-pressed and extruded samples, with little significant region of passivity observed (Fig. 1b). Whilst all samples revealed broadly similar behaviour in the 3% chloride solution, significant differences in corrosion potential and cathodic kinetics were displayed.

3.2. Microstructure of original samples

The morphologies of individual powder particles, as well as particle grain size, are illustrated in Fig. 2. The particles are of irregular shape (Fig. 2a), with grain sizes of about 1–3 μm (Fig. 2b). The surfaces of the powders are covered by oxides of non-uniform thickness. As revealed previously [9], high oxide islands, separated by relatively thinner oxide film regions, usually cover about 30–60% of the surface. The extent of coverage is a function of the atomisation parameters and granulometric composition.

The oxide film on the surface of magnesium-containing powders consists of a mixture of aluminium and magnesium oxides [9]. In-depth distributions of Mg and Zn, determined by AES, are shown in Fig. 3a. The magnesium profile correlates with the oxygen distribution, whereas zinc displays surface depletion. Based on the AES data (Fig. 3a), the width of the region of elemental inhomogeneity is about 50–100 nm.

SIMS measurements qualitatively correlate with AES data (Fig. 3b). The magnesium enrichment and zinc depletion are displayed within a layer of 150–300 nm thickness i.e. approximately three times wider than that determined by AES. This discrepancy arises from the difference in concentration sensitivity between SIMS and
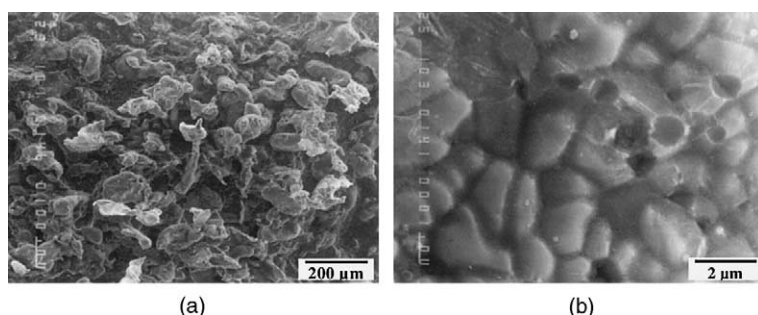

(a)   (b)

Fig. 2. Scanning electron micrograph of water atomised powder particles: (a) irregularly-shaped particles; (b) increased magnification micrograph, revealing the grain size.
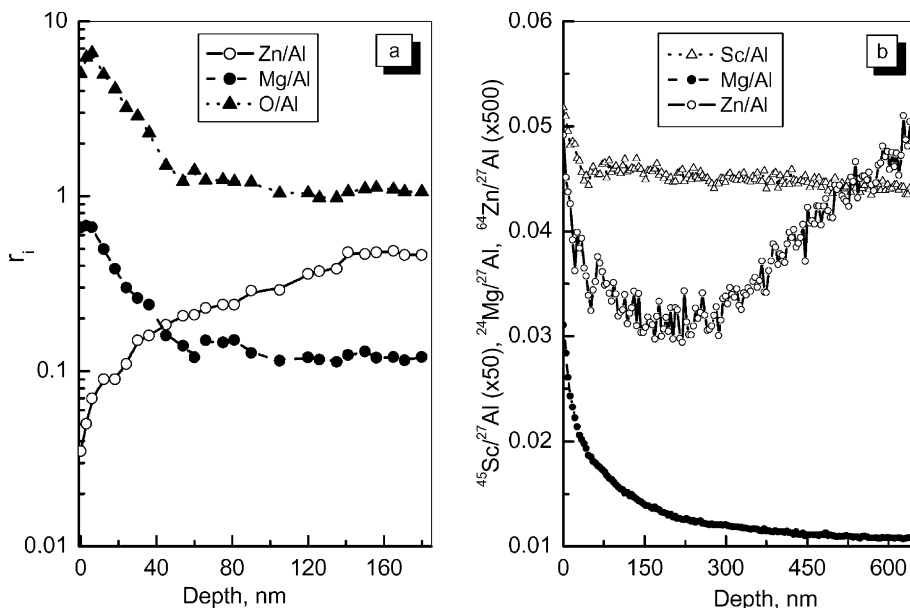
Fig. 3. (a) Variation of Auger peak height ratios with sputter time and (b) typical SIMS secondary ion depth profiles for $^{24}Mg^+$, $^{45}Sc^+$ and $^{64}Zn^+$ ions normalised to $^{27}Al^+$.

AES as discussed by Krajnikov et al. [10]. Briefly, if a peak intensity changes markedly with ion sputtering, SIMS provides more realistic depth profiles over a wide concentration range compared with AES. The sensitivity of SIMS also allowed recording of the scandium profile in the powder subsurface layers (Fig. 3b), which displays a flat profile with a very narrow region of enrichment just beneath the surface.

Grain and subgrain structures of the powder are revealed in polished cross sections of the cold-pressed sample (Fig. 4a). Individual grains form a well-defined dendritic structure. The microstructure parameters, such as interdendrite spacing,
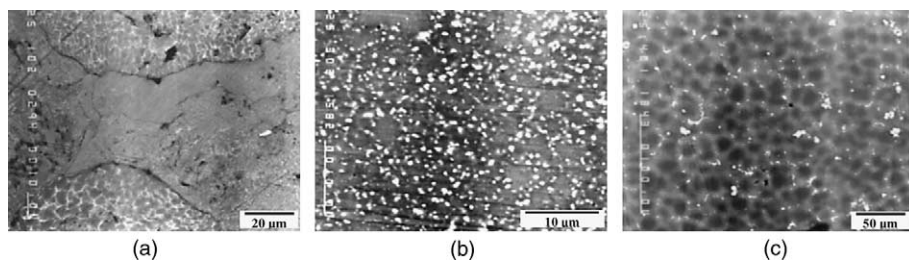

Fig. 4. Scanning electron micrographs of polished metallographic sections of the selected alloys: (a) cold-pressed alloy, backscattered electron image; (b) extruded alloy, backscattered electron image; (c) cast alloy, secondary electron image.
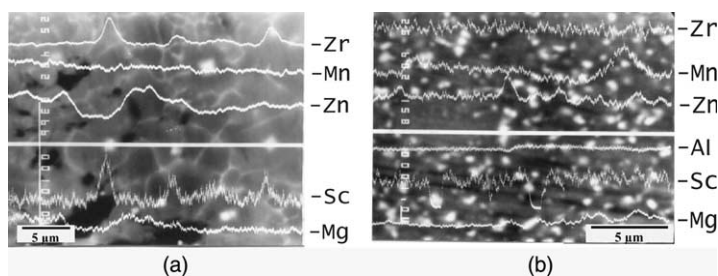
Fig. 5. Backscattered electron micrographs of the RS alloys: (a) cold-pressed alloy, with elemental distributions revealed; (b) extruded alloy, with elemental distributions shown.

and precipitate size and density, depend on the cooling rate. For example, individual particles differ in precipitate density, as displayed in Fig. 4a. Coarse particles usually experience relatively slow cooling rates and thus show high precipitate densities. Two principal types of precipitates are evident in the alloy (Fig. 5a), which are revealed as bright spots or as a net of bright layers because their high average atomic numbers relative to the matrix.

From Fig. 5a, the precipitate containing zinc and magnesium forms a network of layers located along the interdendrite boundaries. The interdendrite zinc and magnesium concentrations, from EDS analysis, can reach 19–20 and 24–25 wt.% respectively, corresponding to three- and eight-fold enrichments from the bulk concentration. The width of the enrichment zone correlates with structure refinement, being undetected in areas of the particle that are cooled at high rates and extending to about 100 nm in areas solidified at reduced rates. Evidently, if precipitated layers are relatively wide, then the precipitated Mg–Zn phase occupies a high volume that causes zinc and magnesium depletion from the bulk. The backscattered electron images reveal a relatively dark matrix within areas of intense precipitation of the Zn–Mg base phases compared with other areas. Other particles, which are of spherical shape and are located mainly within grains, are enriched with zirconium and scandium.

The structure of the extruded material shows a pore-free matrix with many fine precipitates which are usually smaller (0.5 μm) than those in the cold-pressed material (Fig. 4b). Similar to the cold-pressed material, Zn–Mg base and Zr–Sc base particles are revealed in BE images and X-Ray profiles (Fig. 5b).

The cast material is shown in Figs. 4c and 6 respectively, with the microstructural parameters of the cast material being coarser than those of PM alloys. Particles, located either at grain boundaries or within the bulk, are clearly evident at the surface of polished sections (Fig. 4c). Intragranular particles exhibit pronounced crystallographic faceting. From the characteristic maps, the second phases located in the bulk are enriched with scandium (Fig. 6b) and zirconium (Fig. 6c), while phases located at grain boundaries are enriched with zinc (Fig. 6d) and magnesium (Fig. 6e).

The microstructural characteristics of all samples are summarised in Table 2. The matrices of the samples differ; in particular, the cold-pressed sample shows a
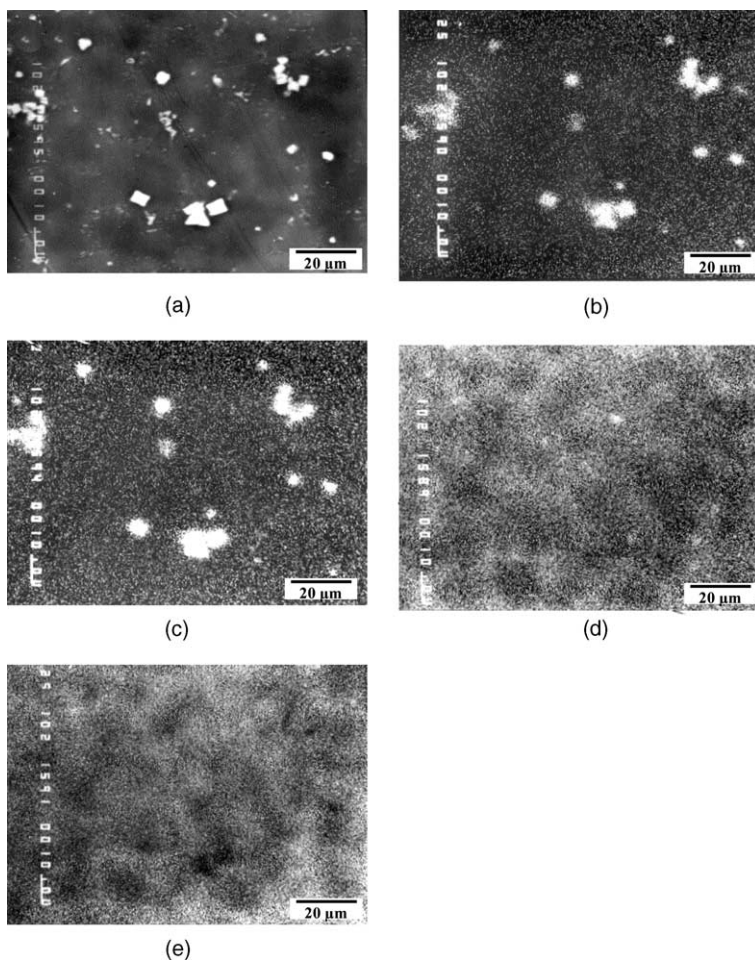
Fig. 6. Secondary electron micrographs of the cast alloy (a—×1000) and associated X-ray elemental mapping at ×1000: (b) Sc_{K_α} map; (c) Zr_{L_α} map; (d) Zn_{K_α} map; (e) Mg_{K_α} map.

Table 2
Typical alloy microstructural parameters

Sample number	Sample	Maximum dendrite spacing (grain size) (µm)	Maximum Sc–Zr precipitate size (µm)
1	Cold-pressed alloy	2–2.5	<1
2	Extruded alloy	1–1.5	0.5
3	Cast alloy	15–20	6–8

dendritic structure that is typical for RS processing. Powder compacting followed by hot extrusion destroys dendrites and forms a typical deformation structure with a grain size of 1–1.5 µm. The cast material exhibits recrystallised grains in the

15–20 μm size range. Zn–Mg and Zr–Sc base precipitate types are evident in all materials. The cast alloy has the coarsest precipitate dispersion, with the extruded alloy showing the finest precipitates.

3.3. Microstructure of samples after corrosion measurements

The microstructure of the cold-pressed material after testing in 3% solution is illustrated in Fig. 7. Corrosion damage is clearly seen in local regions of the polished surface, with the remaining surface evidently unchanged (Fig. 7a). Increased magnification imaging reveals that corrosion proceeds preferentially at some powder particles, with other particles subject to limited corrosion (Fig. 7b). The particles that had suffered corrosion were associated with a high volume fraction of second phase precipitations (Fig. 7b). Importantly, the pores in the cold-pressed material do not change as a result of corrosion.

Further scrutiny of the micrographs allows insight into the corrosion mechanism; thus, a transition layer between the damaged and intact areas of an individual powder particle, subjected to corrosion in 3.0% NaCl solution, is shown in Fig. 7c. The dissolution initiates at the zinc- and magnesium-rich dendrites and then continues with dissolution of the matrix.

The extruded and cast materials behave similarly to the cold-pressed sample manner, Fig. 8a and b illustrate microstructures of the polished samples of extruded and cast alloys respectively after corrosion tests in 3% NaCl solution. A high population density of relatively fine regions of localised corrosion is revealed in the extruded sample. Point by point analysis shows that phases enriched in zinc and magnesium undergo preferential dissolution (Fig. 8a). Scanning electron microscopy reveals that dissolution of the cast material commences at the triple point junctions where the coarsest Zn–Mg phases are located (Fig. 8b). Thus, the Zn–Mg base phases act as a source of local corrosion in both PM and cast samples. No Mg and Zn enrichment of the matrix in a vicinity of the dissolved Zn and Mg phases was detected.
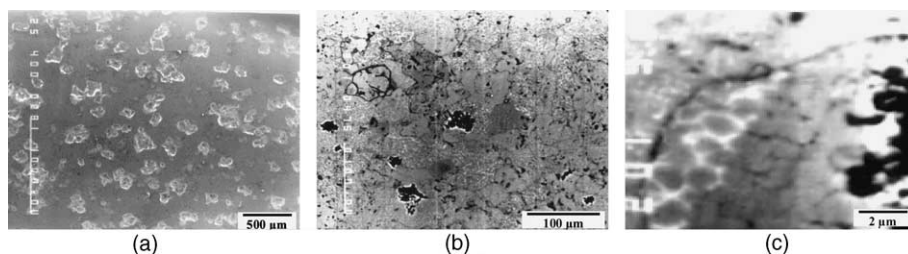

Fig. 7. Scanning electron micrographs of polished metallographic sections of the cold-pressed alloy after full polarisation run in 3% NaCl: (a) secondary electron micrograph showing localised corrosion; (b) backscattered electron image, showing dissolution of individual particles; (c) backscattered electron image revealing the transition layer between the corroded and the non-corroded areas on the surface of an individual particle.
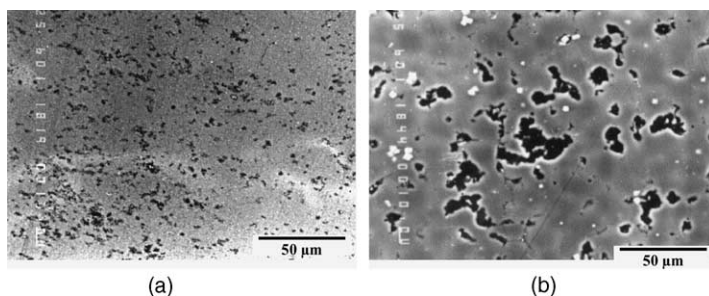
Fig. 8. Scanning electron micrographs of polished metallographic sections of the alloy after full polari-
sation run in 3% NaCl solution: (a) backscattered electron image of the extruded alloy; (b) backscattered
electron image of the cast alloy.

4. Discussion

Significant differences in electrochemical behaviour are observed for polarisation in solutions of low and high chloride concentration. At low chloride concentration, pitting corrosion is observed only in the cast material. At high chloride concentration, both cast and PM materials experience localised corrosion. From microstructural observations, localised corrosion commences with dissolution of the Zn–Mg phases. This contrasts with the corrosion behaviour of the selected materials in water, where corrosion starts with matrix dissolution (Fig. 9). A transition layer of 5–8 μm width is clearly seen between the corroded (dark area from the right side of Fig. 9) and intact (light area from the left side) zones of the polished powder surface. As was found by EPMA, the transition layer is characterised by lower aluminium and higher oxygen concentrations compared with the intact matrix and contains undissolved secondary phases, indicating preferential matrix dissolution in water.

The corrosion behaviour of two PM samples appears generally similar. Both cold-pressed and extruded samples show regions of extensive passivation at low chloride
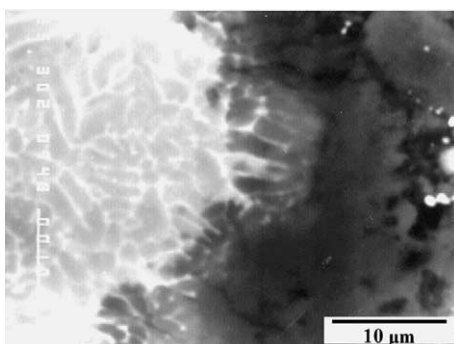

Fig. 9. Backscattered electron image revealing the transition layer between the corroded and non-corroded areas on the surface of an individual particle after oxidation in water.

concentration; such regions are absent at high chloride concentration. The increased corrosion potential and increased cathodic current densities associated with the extruded material result from the increased precipitate population density compared with the cold-phased material. Evidently, RS increases solubility and retains alloying elements in the matrix. Additional heating during consolidation promotes partial precipitation of the secondary phases and thus increases the population density of the precipitates.

A further difference in material structure concerns the presence of pores. The extruded material is pore-free, whereas the cold-pressed powder is associated with 30% porosity. The diameter of pores typically varies from 0.1 to 5 μm. Such porosity, with limited access of oxygen into the pores may act as a site for crevice corrosion during electrochemical measurements that may complicate the interpretation of the results. However, electron-optical examination did not reveal any significant dissolution of the alloy at the surface of the pores, suggesting little contribution to the measured currents.

The AES and SIMS data reveal that the powder surface is covered by a relatively thick layer of aluminium and magnesium-containing oxides. Such a conclusion has been made in other studies [9,11,12] where magnesium was observed to segregate strongly in the surface oxides. While oxidation at room temperature usually yields alumina, the role of magnesium increases with temperature [13–15]. Further, Shimizu et al. [16] has shown co-oxidation of aluminium and magnesium at the alloy/film interface. The faster outward mobility of magnesium cations relative to Al^{3+} cations leads to the formation of crystals of MgO at the surface of the oxide. With time, interfacial roughening develops, possibly associated with spinel formation. The formation of a spinel ($MgAl_2O_4$) at relatively high temperatures (>773 K) has been widely reported [17–19].

Evidently, conditions of water atomisation promote the formation of a relatively thick oxide, which provides improved protection of the surface of the pores formed during atomisation compared with the relatively thin film formed on the polished surface after section preparation at room temperature.

The cast material undergoes localised corrosion at low and high chloride concentration. In contrast to the PM materials, which have higher increased levels of solubility of the alloying elements and more refined second phase precipitation, the cast material contains relatively coarse phases. The precipitation of second phases leads to the formation of galvanic cells with the matrix; the dissolution commences at the very coarse precipitates which are usually located at triple point junctions.

5. Conclusions

1. The intermetallic particles enriched with zinc and magnesium are responsible for initiation of the pitting corrosion in the selected alloys.
2. The improved performance of the PM materials to localised corrosion in 0.3 wt.% NaCl solution compared with the cast material arises because of microstructural differences. The precipitates in the PM materials are significantly refined, and the

difference between the matrix alloying content and that of the precipitates is less than in the cast material.

3. Possible crevice corrosion, associated with pores in the cold-pressed powder, was absent due to formation of protective oxide/oxyhydroxide films on the powder surface during water atomisation.

Acknowledgements

References

[1] I.N. Fridlyander, Wrought Constructional Aluminium Alloys, Metallurgiya, Moscow, 1979 (in Russian).

[2] Yu. Zolotorevsky, Mater. Sci. Forum 242 (1997) 263.

[3] A. Ünal, D.D. Leon, T.B. Gurganus, G.J. Hildeman, in: Production of Aluminium and Aluminium-alloy Powder, vol. 7, ASM International, Ohio, USA, 1998, pp. 148–159.

[4] G.J. Marshall, J. Mater. Sci. 22 (1987) 3581.

[5] O.D. Neikov, Yu.V. Milman, D.B. Miracle, D.V. Lotsko, A.I. Sirko, N.A. Yefimov, in: Proceedings of the European Congress on Powder Metallurgy, vol. 2, Europ. Powd. Metall. Assoc., Bellstone Shrewbury, UK, 2001, pp. 219–224.

[6] O.D. Neikov, D.V. Lotsko, A.I. Sirko, A.V. Sameljuk, G.E. Thompson, N.P. Zakharova, N.A. Yefimov, Properties of rapidly solidified powder alloys of the Al-Zn-Mg system, Mater. Sci. Forum 396–402 (Part 1) (2002) 1223–1228.

[7] K. Kowal, J. DeLuccia, J.Y. Josefowicz, C. Laird, G.C. Farrington, J. Electrochem. Soc. 143 (1996) 2471.

[8] R.M. Rynders, C.-H. Paik, R. Ke, R.C. Alkire, J. Electrochem. Soc. 141 (1994) 1439.

[9] A.V. Krajnikov, M. Gastel, H.M. Ortner, V.V. Likutin, Appl. Surf. Sci. 191 (2002) 26.

[10] A.V. Krajnikov, M. Gastel, H.M. Ortner, Microchim. Acta 138 (2002) 1.

[11] A. Nylund, I. Olefjord, Int. J. Rapid Solidif. 4 (1989) 271.

[12] M. Textor, M. Amstutz, Anal. Chim. Acta 297 (1994) 15.

[13] E. McCafferty, J.P. Wightman, Surf. Interf. Anal. 26 (1998) 549.

[14] G.R. Wakefield, R.M. Sharp, Appl. Surf. Sci. 51 (1991) 95.

[15] C.R. Werret, D.R. Pyke, A.K. Bhattachrya, Surf. Interf. Anal. 25 (1997) 809.

[16] K. Shimizu, G.M. Brown, K. Kobayashi, P. Skeldon, G.E. Thompson, G.C. Wood, Corros. Sci. 40 (1998) 557.

[17] K.J. Holub, L.J. Matienzo, Appl. Surf. Sci. 9 (1981) 22.

[18] C. Lea, J. Ball, Appl. Surf. Sci. 17 (1984) 344.

[19] A. Bahadur, J. Mater. Sci. 22 (1987) 1941.